

Wireless Time and Phase Alignment for Wideband Beamforming in Distributed Phased Arrays

Jason M. Merlo and Jeffrey A. Nanzer

Electrical and Computer Engineering, Michigan State University

Abstract—We present a two node wideband wireless distributed antenna array operating from 3.1–3.3 GHz on software-defined radios (SDRs). To synthesize the total bandwidth of 300 MHz, a 100 MHz bandwidth signal was used over multiple frequency steps, with the carrier frequency re-tuned between each pulse. The nodes were wirelessly synchronized using a high-accuracy two-way time transfer technique which was also used to determine the inter-node range for beamforming. A total beamforming bias \pm standard deviation of 62.46 ± 45.74 ps and $0.27 \pm 2.28^\circ$ at the target beamforming angle at a range of 35.5 m was achieved.

I. INTRODUCTION

Wireless coherent distributed antenna arrays have been gaining interest in recent years for uses ranging from large MIMO apertures [1, TA 5.6.7] to remote sensing and spaceborne observatories [2, TX05.2.6, TX08.2.3]. This is primarily driven by the adaptability, robustness to failure, and reduced costs for certain applications requiring large apertures [3]. Although development of distributed antenna arrays for communication and sensing [3]–[7] is rapidly advancing, there remain challenges in the key areas of wireless time, phase and frequency synchronization. In addition, wireless communication and sensing is undergoing a continuous drive towards higher bandwidth systems to improve communication throughput and sensing resolution. While the motivation for increasing bandwidth is clear, the technical challenges are many, ranging from signal source to antenna. In this paper we investigate the use of wireless time and phase alignment for wideband beamforming in distributed phased arrays.

II. EXPERIMENTAL CONFIGURATION

In a distributed coherent antenna array application, each element in the array must align its time, phase, and frequency in order to ensure coherent reception at the target location. In this work, we utilize a real-time high-accuracy time transfer technique described in [5], which relies on a spectrally sparse two-tone waveform and a two-stage delay estimator to obtain high-accuracy internode delay measurements and compensate for internode time offset and internode range. To correct for signal processing, cable, and antenna-induced time and phase delays, the system was initially calibrated by transmitting orthogonal linear frequency modulation (LFM) waveforms and estimating their inter-pulse time-delay and phase offsets; these were then saved in a lookup table for compensation at runtime. This may be performed separately in practical systems. After the initial calibration, beamsteering was accomplished by adding a time and phase delay to the sampled waveform; this delay included both the calibration delay and phase, as well as

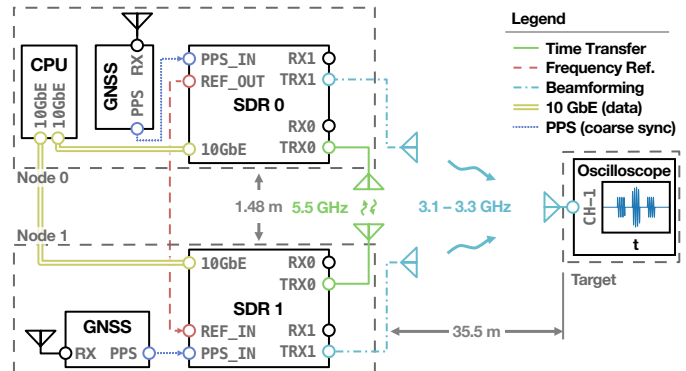


Fig. 1. System schematic. Time synchronization and internode ranging was performed at 5.5 GHz. A pulse-per-second (PPS) signal from a global navigation satellite system (GNSS) receiver was used for an initial coarse time sync on system initialization. Beamforming was performed from 3.1–3.3 GHz. The target oscilloscope was placed 35.5 m downrange.

the delay and phase required to steer the beam to the desired angle given by

$$\tau_{bfi} = \frac{D_i}{c} \sin \theta_{bf} \quad \text{and} \quad \phi_{bfi} = 2\pi f_c \tau_{bfi} \quad (1)$$

respectively, where D_i is the internode distance between the first and i th node, θ_{bf} is the beamsteering angle, and f_n is the beamforming carrier frequency. To synthesize a wider bandwidth than the instantaneous bandwidth of the system, a coherent pulse train of stepped LFM was implemented. Thus, the transmitted waveforms were given by

$$s_i(t) = \sum_{n=0}^N \exp [j\pi(2f_n\tau + k\tau^2) + j\phi_{bfi}] \quad (2)$$

where $\tau = t - t_{TXn} - \tau_{bfi}$, $t \in [-T/2 + t_{TXn}, T/2 + t_{TXn}]$, $k = \pm\beta/T$ is the chirp rate (each node transmitted an up- or down-chirp), defined by chirp bandwidth β over chirp duration T , and N is the number of frequency steps. In this experiment, $\beta = 100$ MHz, $T = 10 \mu\text{s}$, $N = 3$, $I = 2$ and $f_n \in [3.1, 3.2, 3.3]$ GHz. The time between any two pulses in the pulse train t_{TXn} was dictated by the time it took to retune the local oscillator and generate the next waveform in the pulse train—on the computer used in this experiment, this was typically ~ 20 ms.

The hardware used in this experiment, shown schematically in Fig. 1, consisted of two nodes separated by 1.484 m, each with an Ettus USRP X310 SDR controlled by a single desktop computer running GNU Radio 3.10 and UHD 4.3. Each SDR had a sample rate of $f_s = 200$ MSa/s and was connected to the



Fig. 2. Experimental setup. Nodes 0 and 1 are on the left and right, respectively, and the target oscilloscope cart is shown in the inset.

host via 10 Gb Ethernet. To more closely evaluate the performance of timing and ranging, a cable was used for frequency transfer between the nodes in this experiment. A photograph of the configuration is shown in Fig. 2. On initialization, the system used a pulse-per-second (PPS) signal derived from a global navigation satellite system (GNSS) receiver to coarsely align the system to within ~ 100 ns, following which the high-accuracy time-transfer and inter-node ranging process would begin. For the time transfer, each node used log-periodic antennas operating at 5.5 GHz transmitting two-tone pulses with a tone separation of 50 MHz and a duration of $10 \mu\text{s}$ with an signal-to-noise ratio of ~ 36 dB. Finally, the LFM pulse train was transmitted using log-periodic antennas to a Keysight DSOS804A oscilloscope at the target, located 35.5 m downrange, which sampled the waveform at 20 GSa/s using a similar log-periodic antenna. To determine the inter-pulse time and phase delay of arrival, the two orthogonal up- and down-chirp waveforms were matched filtered [8, Ch. 4.2]; the time delay of each was estimated by using quadratic least-squares interpolation to refine the peak estimate, and the phase was estimated using linear interpolation at the location of the corresponding time delay estimate [8, Ch. 7.2].

III. EXPERIMENTAL RESULTS

The measured inter-pulse time and phase arrival estimates at the target are presented for a beamsteering sweep from $\theta_{\text{bf}} \in [0, 50]^\circ$ in Fig. 3. The error between the expected beamforming delay and phase, given by (1), and the measured result at the target is shown in Fig. 4. The vertical dashed red lines in Figs. 3 and 4 indicate the target location $\theta_t = 1.854^\circ$, at which the inter-node time and phase difference bias \pm standard deviation was 62.46 ± 45.74 ps and $0.27 \pm 2.28^\circ$ across all f_n . The internode range estimate during the experiment was $D_1 = 1.40 \text{ m} \pm 2.59 \text{ mm}$ and included a constant range estimation bias of 88 mm which contributed to beamsteering errors at high angles. After compensating for the constant bias, the time and phase difference errors across all angles were 20.47 ± 69.33 ps and $28.13 \pm 21.59^\circ$. This time and phase delay correspond with a maximum beamforming symbol rates and carrier frequencies of ~ 914 MBd at 710 MHz and ~ 1.44 GBd at 3.23 GHz across all angles [3].

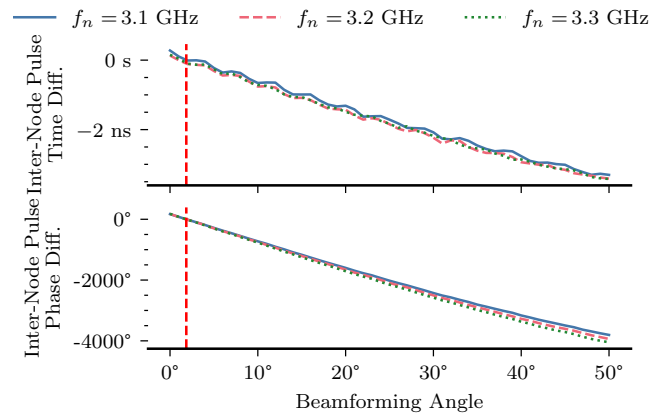


Fig. 3. Measured beamforming results at the target (oscilloscope). The vertical red dashed line indicates the angle where the target was located; at this location the pulse arrival time and phase differences should be zero.

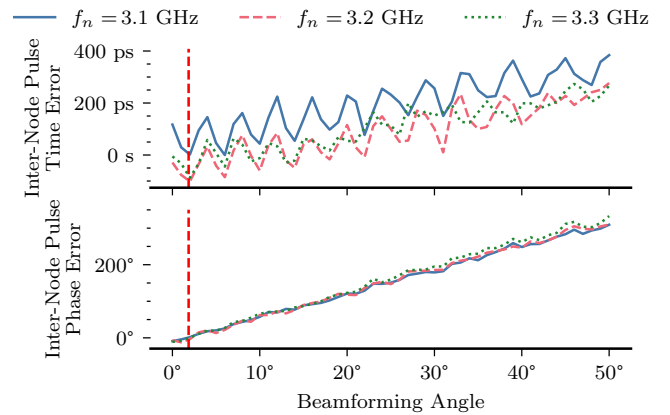


Fig. 4. Error between expected time and phase difference at the target location for a given beamforming angle. The vertical red dashed line indicates the angle where the target was located.

REFERENCES

- [1] "2015 NASA technology roadmaps," National Aeronautics and Space Administration, Tech. Rep., July 2015.
- [2] "2020 NASA technology taxonomy," National Aeronautics and Space Administration, Tech. Rep. HQ-E-DAA-TN76545, Jan. 2020.
- [3] J. A. Nanzer, S. R. Mghabghab, S. M. Ellison, and A. Schlegel, "Distributed phased arrays: Challenges and recent advances," *IEEE Trans. Microw. Theory Techn.*, vol. 69, no. 11, pp. 4893–4907, 2021.
- [4] S. Prager, M. S. Haynes, and M. Moghaddam, "Wireless subnanosecond RF synchronization for distributed ultrawideband software-defined radar networks," *IEEE Trans. Microw. Theory Techn.*, vol. 68, no. 11, pp. 4787–4804, 2020.
- [5] J. M. Merlo and J. A. Nanzer, "Wireless picosecond time synchronization for distributed antenna arrays," *IEEE Trans. Microw. Theory Techn.*, 2022.
- [6] O. Seijo, J. A. López-Fernández, H.-P. Bernhard, and I. Val, "Enhanced timestamping method for subnanosecond time synchronization in IEEE 802.11 over WLAN standard conditions," *IEEE Trans. Ind. Informat.*, vol. 16, no. 9, pp. 5792–5805, 2020.
- [7] J. E. Gilligan, E. M. Konitzer, E. Siman-Tov, J. W. Zobel, and E. J. Adles, "White rabbit time and frequency transfer over wireless millimeter-wave carriers," *IEEE transactions on ultrasonics, ferroelectrics, and frequency control*, vol. 67, no. 9, pp. 1946–1952, 2020.
- [8] M. Richards, *Fundamentals of Radar Signal Processing, Second Edition*. McGraw-Hill Education, 2014.